

Dynamics of Bloch oscillating transistor near the bifurcation threshold

Jayanta Sarkar,¹ Antti Puska,¹ Juha Hassel,² and Pertti J. Hakonen¹

¹*Low Temperature Laboratory, O.V. Lounasmaa Laboratory, Aalto University, P.O. Box 15100, FI-00076 AALTO, Finland*

²*VTT Technical Research Centre of Finland, P.O. Box 1000, FI-02044 VTT, Finland*

(Received 11 January 2013; revised manuscript received 17 April 2013; published 27 June 2013)

The tendency to bifurcate can often be utilized to improve performance characteristics of amplifiers or even to build detectors. The Bloch oscillating transistor is such a device. Here, we show that bistable behavior can be approached by tuning the base current and that the critical value depends on the Josephson coupling energy E_J of the device. We demonstrate current-gain enhancement for the device operating near the bifurcation point at small E_J . From our results for the current gains at various E_J , we determine the bifurcation threshold on the E_J -base current plane. The bifurcation threshold curve can be understood using the interplay of interband and intraband tunneling events.

DOI: [10.1103/PhysRevB.87.224514](https://doi.org/10.1103/PhysRevB.87.224514)

PACS number(s): 85.25.-j, 74.78.-w, 74.78.Na

In small Josephson junctions, charge and phase reveal their conjugate nature in several macroscopic phenomena. The quantum nature of the phase variable (φ) was shown in macroscopic tunneling experiments,¹ while its conjugate relationship to the charge has been shown in many consequent studies.² One of the consequences of the charge-phase conjugate relationship is the Coulomb blockade of Cooper pairs which arises in ultrasmall Josephson junctions having a capacitance (C) in the femtofarad range.^{3,4} Charging energy $E_C = e^2/2C$ and the Josephson coupling energy $E_J(\varphi) = -E_J \cos \varphi$ are the competing energy scales associated with these two variables. Accordingly, the Hamiltonian for the small Josephson junction contains a periodic potential and, hence, Bloch states with band structure appear. These bands are analogous to the conduction electron energy states in solid state physics.^{5,6}

The Bloch oscillating transistor (BOT) is a three-terminal mesoscopic device which is based on the dynamics of the Bloch bands in a voltage-biased Josephson junction (JJ) in a resistive environment.^{7,8} The operation is due to an interplay of coherent Josephson phenomena and Coulomb blockade of charge transport which is controlled by single-electron tunneling events. The device can be viewed as a charge converter of single electrons, induced from the base electrode, into a sequence of N sequential Cooper pair tunneling events, i.e., Bloch oscillations on the emitter terminal with a Josephson junction. The current gain is ideally given by $\beta = 2N + 1$. The number of Bloch oscillations is limited by interband transitions caused by Landau-Zener (LZ) tunneling which depends exponentially on the band gap between the ground and excited states of the Josephson junction. This simple picture has been found to correspond quite well to the measured current gain.⁹

Incoherent tunneling of Cooper pairs and electrons, however, complicates the basic BOT operation. The interaction of tunneling electrons or Cooper pairs with the electromagnetic environment has been demonstrated to be strong in small tunnel junctions, both in the normal and superconducting states.^{10,11} Bias-induced inelastic tunneling rates can strongly modify the internal dynamics and characteristics of BOT, e.g., leading to bifurcation in the BOT operation. Below the bifurcation threshold the probability of the system residing in the lowest Bloch band (the ground state, see Fig. 1) versus higher bands can be smoothly tuned by changing

base current I_B . Above the threshold, two possible dynamical steady-state solutions emerge at fixed I_B .⁹ The existence of a bifurcation point is important as, with proper design, the vicinity of such a point can be employed to improve the characteristics of the BOT. In this paper, we investigate experimentally the bifurcation threshold in the BOT, and demonstrate current-gain enhancement for small- E_J -device operation as the threshold is approached. From our results for the current gains at various E_J , we determine the bifurcation threshold curve on the I_B - E_J plane. The measured transition curve can be qualitatively explained using a simple analytic approach, in which intraband transitions are taken into account phenomenologically, together with the transition rates due to inelastic tunneling.

This paper is organized as follows. In Sec. I, we first outline the basic principles for understanding the electron tunneling dynamics in a Bloch oscillating transistor. We will concentrate on the dynamics near the bifurcation point at which the current gain of the device diverges. Our analytic model is verified using numerics with a similar approach as done in Refs. 8, 9, and 12. Section II will describe sample fabrication and experimental measurement techniques. Experimental results are presented in Sec. III. We will present data on the current gain at various values of Josephson energy, and construct a curve for bifurcation threshold on E_J versus base current plane. The relation of current gain with the distance from the bifurcation point is also studied in detail. In Sec. IV, we discuss our results in the light of analytical and numerical calculations.

I. THEORY

A. Band model of mesoscopic Josephson junctions

In mesoscopic tunnel junctions, the discreteness of charge starts to play a role via the Coulomb energy $E_C = \frac{Q^2}{2C}$, where C is the capacitance of the junction and Q is the charge on the capacitor plates. In quantum theory, charge is described by the operator $\hat{Q} = -i2e \frac{\partial}{\partial \varphi}$, where φ denotes the phase difference of the order parameter fields across the junction. This operator is canonically conjugate to $\hat{\varphi}$, i.e., $[\hat{Q}, \hat{\varphi}] = i2e$. Hence, there is a Heisenberg uncertainty relation $\Delta Q \Delta \varphi \sim 2e$, which implies that the charge and the phase of the superconducting junction can not be defined simultaneously.

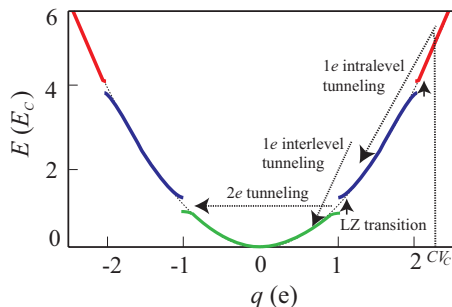


FIG. 1. (Color online) The band diagram of the JJ and the possible transitions. Bloch oscillation follows along the lowest band (green) with a Cooper pair tunneling through the Josephson junction at the end of each period. Landau-Zener transitions to the higher bands, making the Josephson junction Coulomb blocked. Base current relaxes the Josephson junction to its ground state from the excited states.

This leads to delocalization of the phase and to Coulomb blockade of the supercurrent, as experimentally shown by Haviland *et al.*³ in the case when Josephson energy is on the order of the single-electron Coulomb energy, i.e., $E_J/E_C \sim 1$. The same conclusion of delocalization applies even for large values of the ratio E_J/E_C .¹³

Using the differential operator due to the commutation relation, we can immediately write the quantum mechanical Hamiltonian⁶ as

$$H = -E_C \frac{\partial^2}{\partial(\varphi/2)^2} - E_J \cos \varphi. \quad (1)$$

When $E_C \gg E_J$, charge is a good quantum number, which leads to Coulomb blockade of Cooper pairs and a complete delocalization of the phase. Equation (1) then takes the form of the Mathieu equation with the well-known solutions of the form $\Psi_n^q(\varphi) = e^{i\varphi q/2e} u_n(\varphi)$, where $u_n(\varphi)$ is a 2π -periodic function and the wave functions are indexed according to band number n and quasicharge q . Verification of the existence of the energy bands has been carried out by different methods.¹⁴⁻¹⁶ The schematic of a typical band diagram along with different transitions is illustrated in Fig. 1.

Voltage across the junction is given by $V = \frac{\partial E}{\partial q}$ which changes along the energy band when quasicharge is varied. Thus, to have current flowing in the junction, the bias voltage V_C (on the collector, cf. Fig. 2) has to be larger than the maximum Coulomb blockade voltage of the lowest band E_0 : $V_C > \frac{\partial E_0}{\partial q}|_{\max}$. If the current through the junction is low enough, $dq/dt \ll e\delta E_1/\hbar$, where δE_1 is the gap between the first and second bands, the quasicharge q is increased adiabatically, and the system stays in the ground band. The junction is then in the regime of Bloch oscillations; the voltage over the junctions oscillates and Cooper pairs are tunneling at the borders of the Brillouin zone, i.e., here at $q = \pm e$. Consequently, the current through the junction is coherent and the voltage and charge over the junction oscillate with the Bloch oscillation frequency

$$f_B = I/2e, \quad (2)$$

where I is the current through the Josephson junction.

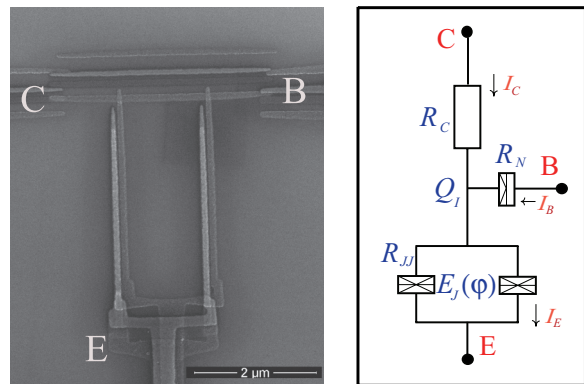


FIG. 2. (Color online) Scanning electron micrograph of the sample (left frame) and a schematic view of the device (right frame). In both pictures, base, emitter, and collector are marked by B, E and C, respectively. Positive directions for the currents are indicated by the arrows. The sample parameters are given in Table I. $Q_I(t)$ is the island charge tracked in the numerical simulations.

If the current I is not adiabatically small, we can have Zener tunneling between adjacent energy bands. The tunneling is vertical, i.e., the quasicharge does not change. The probability of Zener tunneling between bands $n - 1$ and n when $E_C \gg E_J$ is given by

$$P_{n,n-1}^Z = \exp\left(-\frac{\pi}{8} \frac{\delta E_n^2}{n E_C \hbar I}\right) = \exp\left(-\frac{I_Z}{I}\right), \quad (3)$$

where $\delta E_n = E_n - E_{n-1}$ and I_Z is the Zener breakdown current.¹⁷⁻²⁰ Provided that $V_C < \frac{\partial E_1}{\partial q}|_{\max}$ for the excited state E_1 , the junction will become Coulomb blocked on the band E_1 after a Zener tunneling event, and no current will flow through it any more. The role of the base terminal is to relax the Josephson junction back to the ground state where a new sequence of Bloch oscillations can be started. With $E_C \gg E_J$ we can further assume $P_{n,n-1} \approx 1$ for $n > 1$ neglecting Cooper pair tunneling whence we can consider higher bands collectively as a single excited state rendering the system into a two-level system where tunneling from the second to the first band is interlevel and the third to the second band is intralevel tunneling.

B. Incoherent tunneling processes

The external environment gives rise to current fluctuations that couple linearly to the phase variable. These can cause both upwards and downwards transitions. The amplitude of the fluctuations is given by the size of the impedance: the larger the impedance, the smaller are the current fluctuations and the transition rates. As we will see later on, the successful operation of the BOT requires one to control both the upwards and downwards transition rates. When modeling the BOT analytically, we will make use of the Zener transition rates and transitions due to charge fluctuations, both derived in Ref. 13.

The electromagnetic environment around tunnel junctions affects the tunneling process by allowing exchange of energy between the two systems.^{10,21-23} The influence of the external circuit can be taken into account perturbatively, for example, using the so-called $P(E)$ theory.²³ A perturbative treatment of the Josephson coupling term gives rise to a result for

incoherent Cooper pair tunneling^{21,23} where the tunneling electron rate is directly proportional to the probability of energy exchange with the external environment governed by the $P(E)$ function. Taking both positive and negative energy exchange into account, tunneling both inward and outward direction leads to the total current

$$I(V) = \frac{\pi e E_J^2}{\hbar} [P(2eV) - P(-2eV)]. \quad (4)$$

The function $P(E)$ can be written as

$$P(E) = \frac{1}{2\pi\hbar} \int_{-\infty}^{\infty} dt \exp\left[J(t) + \frac{i}{\hbar} Et\right], \quad (5)$$

which is the Fourier transform of the exponential of the phase-phase correlation function

$$J(t) = \langle [\varphi(t) - \varphi(0)] \varphi(0) \rangle. \quad (6)$$

The phase-phase correlation function is determined by the fluctuations caused by the environment and it can be related to the environmental impedance via the fluctuation-dissipation theorem.

For a high-resistance environment, the $P(E)$ function is strongly peaked at energies around E_C , and it may be approximated by a Gaussian function

$$P(E) = \frac{1}{\sqrt{4\pi E_C k_B T}} \exp\left[-\frac{(E - E_C)^2}{4E_C k_B T}\right], \quad (7)$$

where the width is governed by thermal fluctuations in the resistance R_C . Consequently, the subgap IV curve displays a rather well-defined peak centered around $V = 2E_C/e$ due to the $2e$ charge of Cooper pairs. This characteristic feature of the IV curve provides a straightforward way to determine E_J of the investigated devices of small E_J .

The actual downward and upward transition rates $\Gamma_{in\downarrow}(V_C)$ and $\Gamma_{\uparrow}(V_C)$ as a function of the collector voltage were calculated by Zaikin and Golubev.²⁴ The Zener tunneling rate in a resistive environment, and with the assumption $E_C \gg E_J$, is given by

$$\Gamma_{\uparrow} = \frac{v}{2\tau} \exp\left\{-\frac{v_Z}{v-1} \left[1 + \frac{\langle \delta q^2 / e^2 \rangle}{(v-1)^2}\right]\right\}, \quad (8)$$

and the down relaxation rate due to charge fluctuations is given by

$$\Gamma_{in\downarrow} = \frac{v_Z}{\tau \sqrt{2\pi \langle \delta q^2 / e^2 \rangle}} \exp\left\{-\frac{(v-1)^2}{2 \langle \delta q^2 / e^2 \rangle}\right\}, \quad (9)$$

where $v = CV_C/e$, $\tau = R_C C$, $\langle \delta q^2 \rangle = k_B C T$, and

$$v_Z = \frac{\pi^2 R_C}{8R_Q} \left(\frac{E_J}{E_C}\right)^2. \quad (10)$$

The voltage v_Z is related to the so-called Zener break down current by $I_Z = ev_Z/(4\tau)$.

C. BOT modeling near the onset of the bistability

Our present model generalizes the previous analytic BOT theories^{8,25} by including the effect of intraband transitions. The circuit schematics for the basic BOT modeling is depicted in Fig. 2. The basic circuit elements are either a Josephson

junction or SQUID structure at the emitter with a total normal-state tunnel resistance of R_{JJ} , the single tunnel junction at the base with the normal-state resistance R_N , and the collector resistance R_C . The BOT base is current biased via a large resistor R_B at room temperature. In this configuration at constant I_B , there are two solutions of V_B when the system is in the bistable region. On the contrary, for a voltage-biased base, V_B is fixed and no bistability in this situation.²⁶

As required by the $P(E)$ theory, our basic modeling is valid provided $E_J P(2eV) \ll 1$. The intrinsic relaxation is detrimental for BOT operation and, thus, the fluctuations should be kept low by requiring that $R_C \gg R_Q = h/4e^2$. In practice, we need $R_C \gtrsim 100R_Q$ to be close to the presumed idealized operation. Experimentally, this is quite hard to realize though (see Sec. III).

Numerical analysis is needed to calculate properly the characteristics of the BOT devices near the onset of bistability. However, by introducing a phenomenological variable that describes the average number of the tunneling events $\langle N_e \rangle$ before a downward transition is triggered by the base electrons,¹² we may derive a rather simple description for the operation of the BOT. A value of $\langle N_e \rangle \gg 1$ is facilitated by intraband transitions that basically maintain the bias current of the operating point. Changes in the ratio of the bias current and the triggering current can lead to significant changes in the characteristics of the BOT.

As in the earlier analytic descriptions, the BOT emitter current can be thought of as the result of being in either of the following two states: the Bloch oscillation state with a time-averaged constant current and the blockaded state with zero current,

$$I_E = \begin{cases} V_C/R_C, & \tau_{\uparrow} = 1/\Gamma_{\uparrow} \\ 0, & \tau_{\downarrow} = 1/(\Gamma_{in\downarrow} + \Gamma_B/\langle N_e \rangle). \end{cases} \quad (11)$$

The amount of time the system spends in each state is given by the Zener tunneling rate Γ_{\uparrow} , the intrinsic relaxation $\Gamma_{in\downarrow}$, and the quasiparticle tunneling rate Γ_B ; only every $\langle N_e \rangle$ th of the injected base electrons is able to make a downward transition. The base current, however, flows during the opposite times:

$$I_B = \begin{cases} 0, & \tau_{\uparrow} = 1/\Gamma_{\uparrow} \\ e\Gamma_B, & \tau_{\downarrow} = 1/(\Gamma_{in\downarrow} + \Gamma_B/\langle N_e \rangle). \end{cases} \quad (12)$$

From these equations we can simply derive the average emitter and base currents

$$\langle I_E \rangle = \frac{V_C}{R_C} \frac{\tau_{\uparrow}}{\tau_{\uparrow} + \tau_{\downarrow}}, \quad (13)$$

$$\langle I_B \rangle = e \frac{\langle N'_e \rangle}{\tau_{\uparrow} + \tau_{\downarrow}}, \quad (14)$$

where we have defined

$$\langle N'_e \rangle = \frac{\langle N_e \rangle}{1 + \frac{\Gamma_{in}}{\Gamma_B} \langle N_e \rangle}. \quad (15)$$

By combining these two equations, we may write

$$\langle I_E \rangle = \frac{V_C}{R_C} \frac{\tau_{\uparrow}}{e \langle N'_e \rangle} \langle I_B \rangle. \quad (16)$$

Now, when calculating the current gain $\beta_E = \frac{\partial \langle I_E \rangle}{\partial \langle I_B \rangle}$, $\langle N_e' \rangle$ has to be considered as a function of $\langle I_B \rangle$. Thus, we obtain

$$\beta_E = \frac{V_C}{R_C} \frac{\tau_\uparrow}{e \langle N_e' \rangle} - \frac{V_C}{R_C} \frac{\tau_\uparrow}{e \langle N_e' \rangle^2} \frac{\partial \langle N_e' \rangle}{\partial \langle I_B \rangle} \langle I_B \rangle, \quad (17)$$

which can equivalently be written as

$$\beta_E = \frac{V_C \langle I_B \rangle \tau_\uparrow (\tau_\uparrow + \tau_\downarrow)}{R_C e^2 \langle N_e' \rangle^2} \frac{1}{1 - \beta_H}, \quad (18)$$

with

$$\beta_H = \frac{\tau_\uparrow + \tau_\downarrow}{\langle N_e' \rangle} \frac{\partial \langle N_e' \rangle}{\partial \tau_\downarrow} = \frac{e}{\langle I_B \rangle} \frac{\partial \langle N_e' \rangle}{\partial \tau_\downarrow}. \quad (19)$$

With $\beta_H \ll 1$, increasing I_B merely changes τ_\downarrow thus decreasing the time spent in the excited state and consequently enhancing the emitter current. When β_H approaches unity, the gain is further enhanced through the additional effect of I_B in the intralevel tunneling and intrinsic relaxation, the information of which is contained in $\langle N_e' \rangle$. At $\beta_H = 1$, the gain diverges, marking a point where an infinitesimal change in I_B makes the system to undergo a transition from a dynamical state where it is mostly in the ground state to a dynamical state where it is mostly in the excited state rendering the system bistable. With $\beta_H \geq 1$, two stable solutions are available and the operation becomes bistable as observed both experimentally and numerically. Hence, we may consider β_H as a parameter controlling the proximity of the bifurcation threshold.

For $\beta_H \rightarrow 1$, we obtain a linear dependence between β_E^{-1} and $\langle I_B \rangle$ as given by

$$\beta_E^{-1} = \left[\frac{R_C}{V_C} \frac{e^2 \langle N_e' \rangle^2}{\tau_\downarrow (\tau_\uparrow + \tau_\downarrow) \langle I_B \rangle^2} \left(-\langle I_B \rangle - \epsilon \frac{\tau_\uparrow}{\tau_\downarrow} \right) \right] \quad (20a)$$

$$= \left[\frac{R_C}{V_C} \frac{\tau_\uparrow + \tau_\downarrow}{\tau_\downarrow} (-\langle I_B \rangle + I_{B-H}) \right], \quad (20b)$$

where $\epsilon < 0$ is a phenomenological parameter to account for the variation of $\partial \langle N_e' \rangle / \partial \langle \tau_\downarrow \rangle$ under various biasing conditions (see Appendix A). The latter term in the parentheses of Eq. (20a) specifies the threshold current I_{B-H} for the bifurcated, hysteretic threshold. By substituting $\langle I_B \rangle$ from Eq. (14) to the prefactor of Eq. (20a), $\langle N_e' \rangle^2$ and $\langle I_B \rangle^2$ terms cancel each other leaving the prefactor with $(R_C/V_C)(\tau_\uparrow + \tau_\downarrow)/\tau_\downarrow$. The detailed derivation of the analytic formulation is outlined in Appendix B.

Using a simple approximation for the variation of $\langle N_e' \rangle$ with τ_\downarrow , we may derive an analytic formula for the bifurcation threshold on the E_J versus $\langle I_B \rangle$ plane (see Appendix A). The E_J dependence of I_{B-H} comes mainly from Eq. (8), which leads to the analytic form given by

$$\frac{I_{B-H}}{e} \propto \frac{\Gamma_{se\uparrow} + \exp(-\kappa E_J^2)}{\sqrt{1 + \Gamma_B^2/E_J^4}}, \quad (21)$$

where the first term in the numerator $\Gamma_{se\uparrow}$ is the upward transition rate due to single electron tunneling, whereas the second term arises due to LZ tunneling. The parameter κ involves all the other parameters inside the exponent of Eq. (8). This functional dependence between I_{B-H} and E_J in Eq. (21)

is also in good agreement with the results of our numerical simulations.

The BOT behavior described here is referred to as ‘‘normal’’ operation. In this configuration, the junction is initially in the upper band and quasiparticle tunneling due to base current will bring the junction to the lowest band where it performs Bloch oscillations. This coherent oscillation will be inhibited by Zener tunneling and the system jumps back to the upper state and the whole process is repeated again. If the sign of V_C (and consequently I_E) is reversed, the base current will induce transitions to the upper band, an operational mode that we call ‘‘inverted’’ operation. Since the normal operation is conceptually clearer, we have concentrated our studies in this mode of BOT.

II. FABRICATION AND MEASUREMENT

The BOT samples employed in this work were fabricated using a 20-nm-thick Ge mask on top of LOR 3B resist. Patterning of the Ge layer was performed using conventional e -beam lithography at 20 keV. After patterning, the PMMA layer was developed in MIBK:IPA (1:3) solution and subjected to a plasma etch with CHF_4 plasma. Finally, the LOR under the germanium was etched in oxygen plasma up to the desired extent of undercut.

Shadow angle evaporation at four different angles was employed to generate the structures consisting of three metals. Originally, the BOT was envisioned to have a normal-insulator-normal (NIN) junction as the base junction, but the technique of fabricating both superconductor-insulator-superconductor (SIS) and NIN junctions on the same sample is exceedingly difficult and, therefore, we opted to have a NIS base junction instead. The SIS junction is formed of two Josephson junctions in the SQUID geometry; this facilitates tuning of the Josephson energy by magnetic flux. The process order in the evaporation sequence was (I) chromium, (II) aluminum, (III) oxidization, (IV) aluminum, and (V) copper. NMP or PG remover was used for liftoff. Oxidation was done in Ar:O₂ (6:1) mixture at 80 mTorr for 1 min.

A typical sample used in this study is displayed in Fig. 2. The area of the SIS junctions is $100 \times 150 \text{ nm}^2$ each (equal areas within 10%). The NIS junction on the base has an area $70 \times 100 \text{ nm}^2$, roughly half of the SQUID junctions. The measurements were done on a plastic dilution refrigerator (PDR-50) from Nanoway Ltd. The base temperature of the refrigerator was 50 mK. The filtering in the PDR consisted of 70-cm-long Thermocoax cables on the sample holder and 1 kOhm series resistors at 1.5 K. In addition, microwave filters from mini-circuits (BLP 1.9) were used at the top of the cryostat.

The measurement setup in this work was similar to that described in Ref. 27. The BOT base was dc current biased by a resistor $R_B = 1\text{--}10 \text{ G}\Omega$, which was located at room temperature. Voltages were measured with low-noise LI-75A voltage preamplifiers while currents were monitored using DL1211 low-noise current amplifiers.

The resistance values of the three circuit branches were determined at 4.2 K. Since there was a weak temperature dependence in R_C , we determined the actual value from $1/\sqrt{V}$ asymptote²⁸ of the IV curves measured at low E_J .

TABLE I. BOT parameters for the measured sample. R_N and R_{JJ} are the normal-state resistances of the NIS and JJ tunnel junctions in the SQUID-loop geometry, respectively. Resistances are given in units of $k\Omega$ and energies in μeV .

BOT No.	R_N	R_{JJ}	R_C	E_J	E_J^{min}	E_C	Δ
1	53	27	550	17	2.7	40	150
2	75	21	305	25	3.3	60	165

The maximum Josephson energy E_J was calculated using the Ambegaokar-Baratoff relation which yielded $E_J = 17 \mu\text{eV}$. The flux-modified Josephson energy was obtained from the formula $E_J(\Phi) = E_J \sqrt{\cos^2(\pi\Phi/\Phi_0) + d^2 \sin^2(\pi\Phi/\Phi_0)}$, where $d = \frac{E_{J_1} - E_{J_2}}{E_{J_1} + E_{J_2}}$ denotes the asymmetry in Josephson energies between the two SQUID loop junctions with E_{J_1} and E_{J_2} , respectively. By fitting $E_J(\varphi)$ to the measured IV curves, we found $d = 0.15$ and 0.13 for samples No. 1 and No. 2, respectively. Emitter-collector and base-emitter IV curves were employed to determine the effective energy gap Δ of the samples (see Table I), which is 20–30 μeV smaller than the bulk value $\Delta = 0.18 \text{ meV}$. This reduction of the gap is presumably due to the inverse proximity effect²⁹ due to the chromium resistors. The spatial variation of the inverse proximity effect would also explain the larger asymmetry between the SQUID junctions than is expected due to the difference in their areas.

III. EXPERIMENTAL RESULTS

A. IV characteristics

IV characteristics of sample No. 1 measured at a few magnetic flux values are illustrated in Fig. 3: the emitter-collector current I_E is recorded as a function of V_C at $I_B = 0$. The data clearly show Coulomb blockade of supercurrent^{3,4} at all investigated values of the Josephson coupling energy. The peak in the IV in the subgap region is a signature of the inelastic Cooper pair tunneling, commonly referred to as $P(E)$ peak

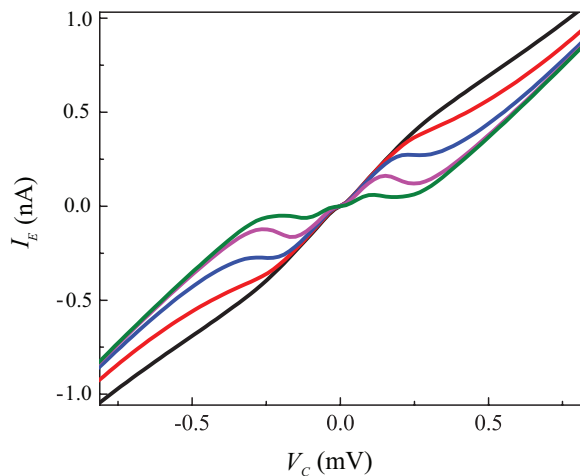


FIG. 3. (Color online) IV characteristics of sample No. 1 at a few values of Josephson coupling energy: $E_J = 9 \mu\text{eV}$ (black line), $7.3 \mu\text{eV}$ (red line), $6 \mu\text{eV}$ (blue line), $4.5 \mu\text{eV}$ (magenta line), and $2.8 \mu\text{eV}$ (green line), without base current ($I_B = 0$) at $T = 90 \text{ mK}$.

[cf. Eq. (7)]. The weakness of the blockade in Fig. 3 is assigned to the small Coulomb energy $E_C = 40 \mu\text{eV}$, the value of which is determined from the position of the $P(E)$ peak, extrapolated to $E_J = 0$. At larger bias voltages, Zener tunneling to higher bands takes place, which causes the phase fluctuation theory to break down. Our results on Zener tunneling are similar to those of Kuzmin *et al.* who investigated a single Josephson junction in an environment of chromium resistor.³⁰

Figure 4 demonstrates the effect of the base current on the IV of the BOT. The normal and inverted operation regions are defined by sign combinations $(V_C, I_E, -I_B)$ and (V_C, I_E, I_B) , respectively.⁹ Both the normal and inverted modes of operation display a strong increase in the onset of the LZ tunneling current, which is seen as the movement of the shoulders in the IV curves up to larger currents. The down-turning shoulders in the upper and lower sets of the IV curves are distinct features of LZ tunneling,¹³ while the data at $I_B = 0$ display only smeared bumps of these features. This enhancement of the LZ current suggests that effectively the energy gap between the ground and excited states is increased due to the noise induced by the current in the base junction. The shoulders move even further apart with growing base current, which indicates an increase in the effective energy gap at the Brillouin zone boundary. In general, the inverted operation displays comparable characteristics as the normal operation, but we found that bistable behavior appeared at smaller bias currents in the inverted regime compared with the normal operation mode; in some cases, these modes differed by a factor of 4 in the base current for bifurcation threshold. This difference in the required base currents for bifurcation threshold is seen in the simulations as well. Nonetheless, since the normal operation appears to provide more clear-cut data, we concentrated our studies on this operating regime.

B. Gain determination

Figure 4(b) displays a basic set of data for current gain determination in the normal operating region. Emitter current I_E is depicted as a function of collector voltage V_C at eight values of base currents I_B . The regime with a large negative slope marks the active bias regime of the BOT amplifier. The steepest monostable curve [the second one from left at $I_B = 0.095 \text{ nA}$ in Fig. 4(b)] has a narrow linear regime in the center of the negative slope part, the width of which amounts to about 2 pA in I_B . This corresponds to the maximum dynamic range in I_B over which the BOT has substantial current gain at this bias point. Roughly, a change in the base current by $\Delta I_B = 2 \text{ pA}$ corresponds to 50 pA in I_E , and the current gain becomes $\beta_E = 25$. Eventually, the slope of the IV diverges with increasing I_B , after which the IV characteristics become hysteretic as seen at the largest value of $I_B = 0.105 \text{ nA}$ in Fig. 4(b). Clearly, in the BOT operation near the divergence point, the dynamic range is inversely proportional to the current gain.

We have checked that bifurcation does not depend on the value of the current bias resistor in the range 10^8 – $10^{10} \Omega$. Moreover, we have performed simultaneous transconductance $g_m = \frac{\Delta I_E}{\Delta V_B}$ and current gain measurements to determine the input impedance of the BOT $Z_{in} = \frac{\Delta V_B}{\Delta I_B} = \frac{\Delta V_B}{\Delta I_E} \times \frac{\Delta I_E}{\Delta I_B} = \frac{\beta_E}{g_m}$. We find that the input impedance diverges at the same point as the gain.

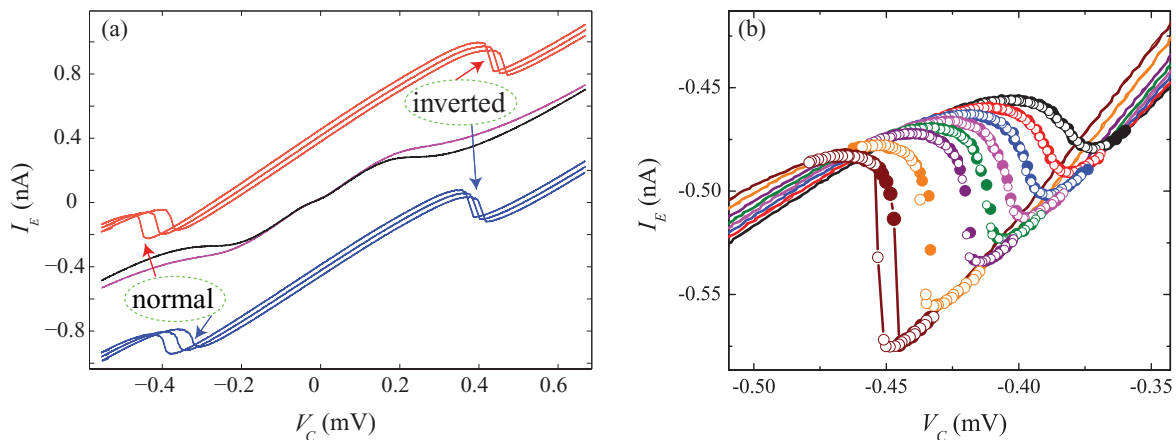


FIG. 4. (Color online) (a) Middle traces: magenta and black IV curves are measured without base current at $E_J = 6.5$ and $5.8 \mu\text{eV}$, respectively. Red curves, corresponding to $E_J = 6.5 \mu\text{eV}$, are measured at $I_B = +0.3, +0.34,$ and $+0.38 \text{ nA}$ (traces from right to left). Blue curves have the same bias conditions as the red curves but were measured at $E_J = 5.8 \mu\text{eV}$. The red curves are offset by $(+0.22 \text{ mV}, +0.42 \text{ nA})$ for clarity, like the blue curves by $(+0.22 \text{ mV}, -0.42 \text{ nA})$. (b) The normal operation region of the BOT at $E_J = 7.1 \mu\text{eV}$ with increasing I_B . Negative slope is the Landau-Zener tunneling regime, increases with I_B and eventually the slope diverges: $I_B = +0.06, 0.065, 0.07, 0.075, 0.08, 0.085, 0.095,$ and 0.105 nA (from right to left). Filled (open) circle traces are of I_E when V_C is swept from left (right) to right (left). The measurement temperature was at $T \sim 90 \text{ mK}$.

According to basic BOT theories,^{7,12,25} the current gain is independent of the base current. However, the situation changes near the bifurcation point. This is because there can be two different kinds of base current components: one comprising of tunneling events causing interband transitions (the only component in the traditional BOT base current) and another one leading only to intraband events. Only the interband transitions lead to gain in the BOT, while the intraband transitions are to maintain the bias current. As the base current grows, the ratio of these two current components may change with increasing I_B which leads to current dependence of the gain and, eventually, to the diverging behavior when approaching the bistability point. Hence, the observed strong increase in β_E with increasing base current is a sign of the operation near the bifurcation point where the gain grows according to Eq. (20).

In addition to the analysis of data as in Fig. 4(b), we have measured the current gain using traces of I_E versus I_B as illustrated in Fig. 5. The figure displays data at five different values of the V_C at $E_J = 7.1 \mu\text{eV}$. The current gain is calculated from the negative slope of I_E - I_B traces: $\beta_E = -\frac{\Delta I_E}{\Delta I_B}$. The steepest negative slope yields the optimum current gain, which we determined as an average of the up and down I_B sweeps. At large gains, there was often a rather large difference (\sim factor of 2) between the gains of up and down sweeps. In such cases, we considered the operation of the BOT bistable at these bias points and disregarded the larger gain values that would have been obtained from these sweeps (not shown in Fig. 6). When $\beta_E > 50$, the gain determinations became problematic because of $1/f$ noise and creep in the measurement, which gradually took the device out of the linear regime during the gain determination.

Figure 6 depicts data on the inverse of β_E versus I_B which were obtained from the analysis of $I_E(I_B)$ scans performed in the range with $E_J = 4.6$ – $10.5 \mu\text{eV}$. A data point in Fig. 6 corresponds to the maximum slope determined from a single

I_E - I_B trace illustrated in Fig. 5. Similarly, at different V_C values (different traces in Fig. 5) we determined maximum β_E 's and the corresponding I_B 's for different E_J values to generate Fig. 6. With increase in I_B , the maximum β_E increases and eventually diverges at the bifurcation threshold. Plotting β_E^{-1} makes the analysis of the diverging gain regime simpler and allows us to examine the vicinity of the bifurcation point where we are supposed to have $\beta_E^{-1}(I_B) \rightarrow 0$.

Experimentally, the problem in this region arises because the dynamic range becomes zero and measurements without

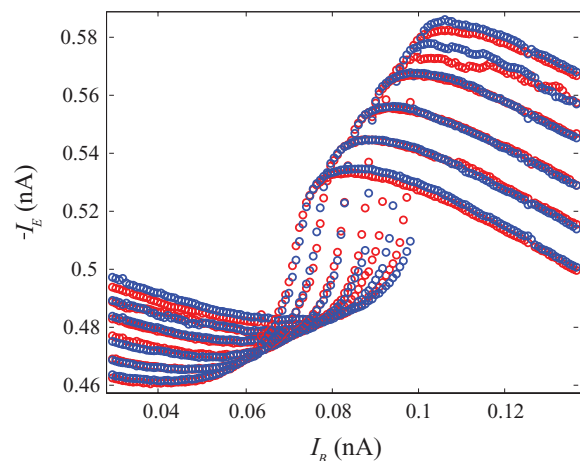


FIG. 5. (Color online) Measurement of the current gain by tracing I_E vs I_B at $E_J = 7.1 \mu\text{eV}$. The steepest slope yields the operating point with the largest current gain β_E at the corresponding collector voltage V_C . Traces were measured at $T = 90 \text{ mK}$ using $V_C = -0.443, -0.429, -0.419, -0.410,$ and -0.401 mV (traces from right to left). Different signs of I_E and I_B correspond to the regime of normal operation. Red (purple) traces are for growing (decreasing) sweep of I_B .

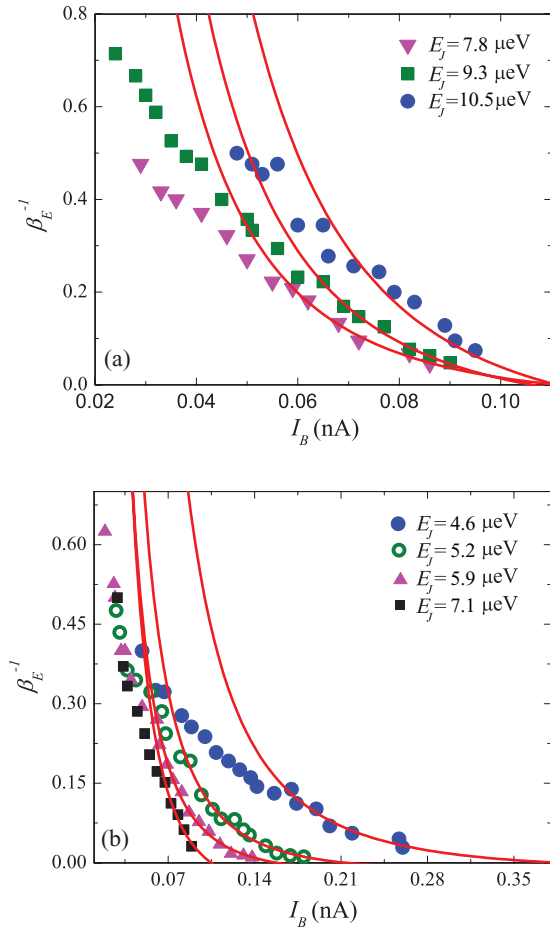


FIG. 6. (Color online) Inverse gain $1/\beta_E$ as a function of bias current I_B . Each data point was obtained from a I_E vs I_B sweep illustrated in Fig. 5. The solid curves were obtained using Eq. (20) fitted to the highest I_B quartile fraction of the data sets (first to eighth lowest β_E^{-1} values).

noise-induced smearing become impossible. Nevertheless, the data in Fig. 6 display how the critical regime is approached at $\beta_E^{-1} > 0.02$ which corresponds to our highest reliable gain values. All of the data at small values of β_E^{-1} are seen to show a nearly linear dependence on I_B , especially at large values of Josephson energies. At our smallest value of $E_J = 2.7 \mu\text{eV}$ (sample No. 1), we could not reach the bistable regime at all. The theoretical dependence for $\beta_E^{-1}(I_B)$, illustrated by red curves in Fig. 6, were obtained by fitting Eq. (20a) to the data just near the divergence point, as required by its regime of validity.

C. Bifurcation threshold

The experimentally determined values of I_{B-H} for the bifurcation point are plotted in Fig. 7 on the I_{B-H} - E_J plane. The plot was generated from the fits in Fig. 6 by selecting the points of $\beta_E^{-1}(I_{B-H}) = 0$. Figure 7 indicates that the onset of bistability is nearly independent of base current at large values of E_J , while a steep increase in I_{B-H} is observed below $E_J = 6 \mu\text{eV}$. The observed behavior is quite well reproduced

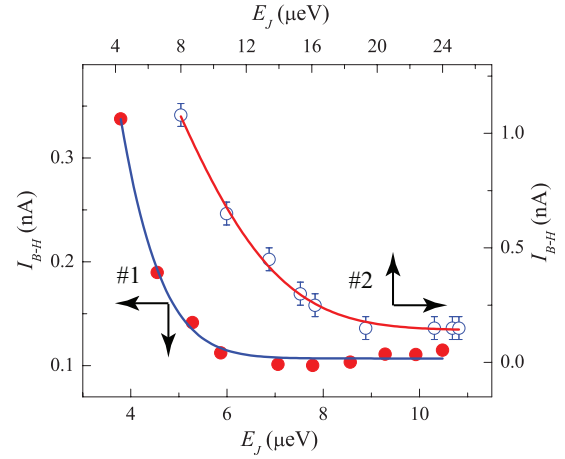


FIG. 7. (Color online) Bifurcation threshold on the E_J vs I_B plane. Red (filled) and blue (open) circles denote the I_{B-H} values for the samples No. 1 and No. 2, respectively. Solid curves display the theoretical dependence from Eq. (21).

by our phenomenological formula in Eq. (21) which is depicted by the solid curve.

For sample No. 2, we found a similar threshold curve which indicates that the bifurcation behavior and its dependence on E_J is a fundamental characteristic of the Bloch oscillating transistor. The bifurcation threshold curves for both the samples are depicted in Fig. 7. For sample No. 2, the bifurcation threshold current is higher than that for sample No. 1. From the fitted curves we found that κ [see Eq. (21)] for sample No. 1 is higher than for sample No. 2 which comes from the fact that κ contains term R_C which is higher in sample No. 1 than in sample No. 2. The smaller base current needed for bifurcation for sample No. 1 than in comparison to sample No. 2 is accounted from the fact that β_H for sample No. 1 is higher than for sample No. 2. Absence of bifurcation was observed in both samples No. 1 and No. 2 at their respective lowest E_J values.

The rate ($\frac{\Delta\beta_E^{-1}}{\Delta I_B}$) at which $1/\beta_E$ reaches the bifurcation point depends on E_J as seen from Fig. 8(a). Initially, the slope increases rapidly with E_J up to $6 \mu\text{eV}$, while between 6 – $10.5 \mu\text{eV}$ the slope appears to be saturated. In this region, the bifurcation threshold current is almost independent of E_J (cf. Fig. 7). The slope variation over the whole range of E_J amounts to a factor of 5.5. Hence, the variation of E_J does not necessarily change β_E strongly, which is a desirable property concerning $1/f$ noise due to critical current fluctuations.

Theoretically, the rate $\frac{\Delta\beta_E^{-1}}{\Delta I_B}$ is hard to evaluate from Eq. (20). The significant prefactor of Eq. (20b) contains two terms : V_C/R_C and $(\tau_\downarrow + \tau_\uparrow)/\tau_\downarrow$. We have analyzed how $\frac{\Delta\beta_E^{-1}}{\Delta I_B}$ varies theoretically with E_J for sample No. 1 by estimating the factor $\frac{R_C}{V_C} \frac{\tau_\downarrow + \tau_\uparrow}{\tau_\downarrow}$. By using Eq. (14), we can relate $\frac{\tau_\downarrow + \tau_\uparrow}{\tau_\downarrow}$ to the experimentally determined quantity $\frac{\langle I_E \rangle}{V_C/R_C}$, while V_C is obtained from the bias voltage, which is increased by 60% over the range of $E_J = 3.9$ – $10.5 \mu\text{eV}$. In Fig. 8(b), we show the variation of $\frac{\tau_\downarrow + \tau_\uparrow}{\tau_\downarrow}$ with E_J as determined for the maximum current (I_E) at the subgap $I(V)$ peak. Together, these opposing contributions result in a change by a factor of 3.3 in $\frac{\Delta\beta_E^{-1}}{\Delta I_B}$, which

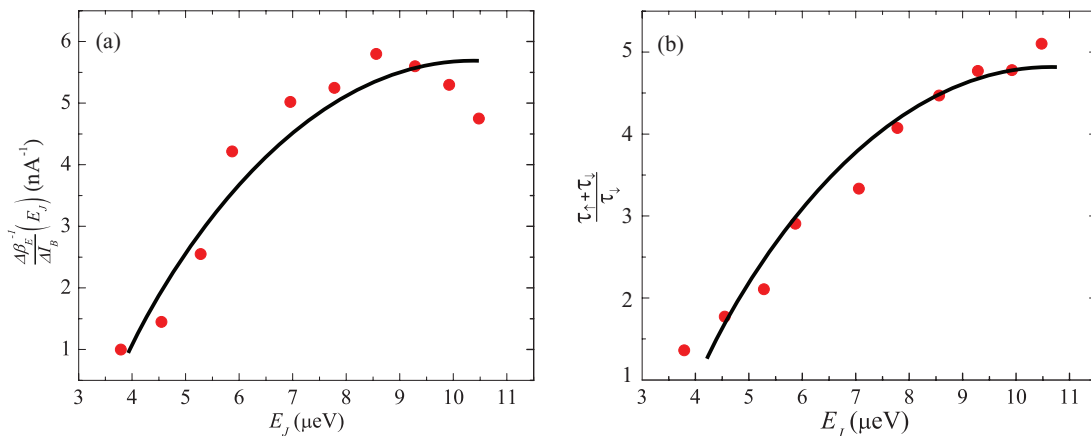


FIG. 8. (Color online) (a) $\frac{\Delta\beta_E^{-1}}{\Delta I_B}$ vs E_J plotted near the bifurcation threshold. Each point at different E_J was derived from fits in Fig. 6. (b) $\frac{\tau_{\uparrow} + \tau_{\downarrow}}{\tau_{\downarrow}}$, deduced from experimentally determined $\frac{\langle N_e \rangle}{V_C/R_C}$, is plotted vs E_J . Solid curves are seen to display the similar character, but the theoretical estimate falls short by 70% from the change in Fig. 8(a).

falls slightly short from the observed factor of 5.5 in Fig. 8(a). Hence, we can conclude that our simple model explains the rate of approach towards the bifurcation threshold with fair extent.

We have also tried to determine the ratio of interband and intraband transitions which is governed by $\langle N_e \rangle$. According to Eqs. (14) and (15), there is the following relation between the base current and $\langle N_e \rangle$: $\langle I_B \rangle = \frac{e\langle N_e \rangle^2}{\Gamma_B} \frac{\tau_{\downarrow}}{\tau_{\uparrow} + \tau_{\downarrow}}$. With the approximation $\langle I_B \rangle \propto \Gamma_B$, we can conclude that $\langle N_e \rangle \propto I_{B-H} \sqrt{\frac{\tau_{\uparrow} + \tau_{\downarrow}}{\tau_{\downarrow}}}$.

From Fig. 8(b), the increase in $\sqrt{\frac{\tau_{\uparrow} + \tau_{\downarrow}}{\tau_{\downarrow}}}$ is ~ 2 whereas from Fig. 7 the decrease in I_{B-H} for sample No. 1 is ~ 4 . Thus, we can conclude that $\langle N_e \rangle$ goes down with increasing E_J . But, unfortunately, we can not determine the exact number of $\langle N_e \rangle$ from this analytical formulation.

In our numerical analysis, we have considered the circuit model used by Hassel *et al.*⁹ and modified it for current bias configuration. Here, we have calculated the island charge as a function of time by taking into account three contributions: charge relaxation through R_C together with the tunnel current through the emitter and base junctions, respectively. The tunnel currents through these junctions are calculated using time-dependent $P(E)$ theory.⁹ In the simulation, $P(E)$ is calculated numerically by considering only the real part of the environmental impedance. The simulation runtime was chosen longer than the time constant due to R_B and the capacitance from base to ground so that the steady state was reached properly. Moreover, we monitored the tunneling events on the island with time, which clearly revealed the Bloch oscillating state and its transition to the higher band. By counting the number of tunneling events when the system undergoes a change from higher band to lower band we could calculate $\langle N_e \rangle$ from the simulation.

IV. DISCUSSION AND CONCLUSIONS

According to the basic theory of the BOT operation, the gain should depend exponentially on E_J/E_C via the tunneling rates Γ_{\uparrow} and $\Gamma_{in\downarrow}$ (Ref. 25) when $E_C \gg E_J$. In this small- E_J limit,

the energy gap between the first two bands is small, which facilitates the use of the up- and down-transition rates [Eqs. (8) and (9)] from perturbation theory. In our experiments, we are well in this limit, which has not been the case in many of the previous measurements, for example, in Ref. 7 the maximum gain of $\beta_E = 35$ was achieved for $E_J/E_C = 3.4$. A current gain of $\beta_E = 25$ was reported for low $E_J/E_C = 0.3$ in Ref. 31.

In our present paper, we have observed a large current gain of ~ 50 even at $E_J/E_C = 0.1$. The estimates from the basic theory²⁵ amount to $\beta_E = 4.8-7$ for $E_J = 5-11.8 \mu\text{eV}$, well below the measured values. Moreover, we did not observe any variation of the maximum gain with E_J , which, together with magnitude of β_E , is consistent with the operation near the bifurcation point where the main gain mechanism has a different origin than in the regular BOT operation. For amplifier operation, the operation near the bifurcation threshold can be used to reduce the equivalent current noise and, consequently, to improve noise matching when measuring objects with characteristic impedance in the range of $> 1 \text{ M}\Omega$.³² The increasing input impedance near the threshold point tends to decrease the bandwidth. In any case, however, the BOT is likely to be most useful in low-noise low-frequency applications.

In the operating regime near the bifurcation point, the base current is a combination of a working point current, not inducing interband transitions, and a significantly smaller part that leads to transitions, the ratio of these two currents being given by the parameter $\langle N_e \rangle$. In our phenomenological modeling with a large number of intraband transitions, the current gain is simply related to $\langle N_e \rangle$ and the upward tunneling rate Γ_{\uparrow} [see Eqs. (15) and (16)]. Hence, a large current gain is expected when approaching a regime where there are two stable solutions for the base current with different values for $\langle N_e \rangle$. When $\langle N_e \rangle$ is large, then almost all of the current is used to just keep the operating point. In our simulation, we find a factor of 15 change in $\langle N_e \rangle$ over the measured range but, unfortunately, our analysis is not able to yield absolute numbers for $\langle N_e \rangle$ from our measured data.

When comparing our findings with the numerical work of Hassel and Seppä,^{8,12} we find a weaker overall dependence

of the device performance on the sample parameters and biasing parameters than was found in the simulations. The weaker overall dependence may, of course, be valid only for the regime of the sample parameters/device configurations that were investigated in this work. Nevertheless, the weaker parameter dependence is an important factor that contributes to the success of the simple phenomenological modeling that we have employed. The weaker overall changes may also indicate that there is external noise present in the measurements and our results should be compared with simulations performed at a higher effective temperature. Furthermore, as an example of the differences, let us point out that if we take the bifurcation threshold parameter from Ref. 12, $\beta_H = 0.02(\frac{R_C}{R_N})^2 \exp[\frac{\pi e^2 R_C}{16\hbar} (\frac{E_J}{E_C})^2]$, we find that our sample No. 1 should be bifurcated at all base currents ($\beta_H \sim 2.4-11.5$). We think that the absence of bifurcation at $I_B = 0$ with β_H well above 1 indicates the necessity to add a capacitance in parallel to R_C into the simulations, which would take into account the parasitic capacitance component on the sample chip. This parasitic capacitance will influence the Coulomb blockade at large frequencies, at which it will reduce the real part of the impedance seen by the Josephson junction.

In conclusion, we have investigated the dynamics and modeling of the BOT when approaching a bifurcation point governed by intricate interband transition dynamics. Our results present an experimental analysis on the behavior of the BOT in the regime where its behavior is fully governed by switching dynamics with the rates imposed by the biasing conditions. We have reached record-large current gains even though the device was operated just at small Josephson coupling energies $E_J = 2.7-10.5 \mu\text{eV}$. We have mapped a crossover transition diagram on the E_J versus I_B plane and compared its shape to analytic modeling, where the intraband transitions are included in terms of a phenomenological parameter $\langle N_e \rangle$. The same modeling was also successfully applied to describe how the current gain diverges as a function of the base current I_B . Our findings are consistent with the gain divergence as $1/(1-\beta_H)$ where the bifurcation threshold parameter β_H is only weakly dependent of E_J . The weak dependence makes this regime attractive for application where large current gain is needed at low frequencies.

ACKNOWLEDGMENTS

This work has been supported in part by the EU 7th Framework Programme (FP7/2007- 2013, Grant No. 228464 Microkelvin) and by the Academy of Finland through its LTQ CoE grant (Project No. 250280). We thank A. Manninen, M. Paalanen, and H. Seppä for fruitful discussion. We acknowledge Micronova cleanroom facilities for fabrication of our samples. Financial support by Technology Industries of Finland Centennial Foundation and TEKES is gratefully acknowledged.

APPENDIX A: ANALYTICAL DERIVATION OF THRESHOLD CURVE

It is difficult to obtain an analytic expression for the derivative $\partial\langle N_e' \rangle/\partial\tau_\downarrow$ and, hence, we had to be satisfied with

crude approximations. Equation (19) specifies the relation between β_H and the derivative $\partial\langle N_e' \rangle/\partial\tau_\downarrow$ as follows: $\beta_H = \frac{e}{\langle I_B \rangle} \frac{\partial\langle N_e' \rangle}{\partial\tau_\downarrow}$. The partial derivative of $\langle N_e' \rangle$ with respect to τ_\downarrow can be approximated as

$$\frac{\partial\langle N_e' \rangle}{\partial\tau_\downarrow} = \frac{\langle N_e' \rangle}{\tau_\downarrow} + \epsilon, \quad (\text{A1})$$

where $\epsilon < 0$ is a phenomenological correction term. In order to determine the variation of $\langle N_e' \rangle$ with τ_\downarrow explicitly, we follow an interpolative approach using

$$\langle N_e' \rangle = [1 + (\Gamma_B \tau_\downarrow)^2]^{1/2}, \quad (\text{A2})$$

which agrees with the limits; when τ_\downarrow is short (N_e') approaches 1 and $\langle N_e' \rangle \simeq \Gamma_B \tau_\downarrow$ when τ_\downarrow is long. Hence,

$$\frac{\partial\langle N_e' \rangle}{\partial\tau_\downarrow} = \frac{\sqrt{1 + (\Gamma_B \tau_\downarrow)^2}}{\tau_\downarrow}, \quad (\text{A3})$$

which leads to

$$\begin{aligned} \epsilon &= \frac{\partial\langle N_e' \rangle}{\partial\tau_\downarrow} - \frac{\langle N_e' \rangle}{\tau_\downarrow} \\ &= -\frac{1}{\tau_\downarrow \sqrt{1 + (\Gamma_B \tau_\downarrow)^2}}. \end{aligned} \quad (\text{A4})$$

Using Eq. (A1), we can write for the bifurcation threshold parameter

$$\beta_H = \frac{e}{\langle I_B \rangle} \frac{\partial\langle N_e' \rangle}{\partial\tau_\downarrow} \quad (\text{A5})$$

$$= \frac{e}{\langle I_B \rangle} \left[\frac{\langle N_e' \rangle}{\tau_\downarrow} + \epsilon \right]. \quad (\text{A6})$$

Using the expression of $\langle I_B \rangle$ from Eq. (14),

$$\langle I_B \rangle = \frac{e\langle N_e' \rangle}{\tau_\downarrow(1 + \frac{\tau_\uparrow}{\tau_\downarrow})},$$

and substituting it with $\frac{\langle N_e' \rangle}{\tau_\downarrow}$ into Eq. (A6), we get the equation

$$\frac{I_{B-H}}{e} \simeq -\epsilon \frac{\tau_\downarrow}{\tau_\uparrow} \quad (\text{A7})$$

at $\beta_H = 1$. By inserting ϵ from Eq. (A4), we obtain an analytic expression for the bifurcation curve

$$I_{B-H} = \frac{1}{\tau_\uparrow} \frac{1}{\sqrt{1 + (\Gamma_B \tau_\downarrow)^2}}. \quad (\text{A8})$$

The upward transition rate $1/\tau_\uparrow$ depends on both LZ tunneling Γ_\uparrow and single-electron tunneling ($\Gamma_{se\uparrow}$). Single-electron events induced by the base current were found to be important in the simulated time traces of the island charge at high- E_J values. Hence,

$$\frac{1}{\tau_\uparrow} = \Gamma_\uparrow + \Gamma_{se\uparrow}. \quad (\text{A9})$$

According to LZ tunneling (Γ_\uparrow) [cf. Eq. (8)],

$$\Gamma_\uparrow \propto \exp(-\kappa E_J^2), \quad (\text{A10})$$

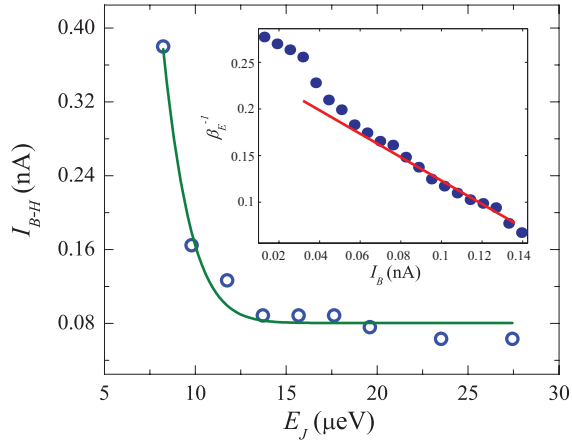


FIG. 9. (Color online) Bifurcation threshold on the E_J vs I_B plane obtained from the simulation. The solid curve is the analytic dependence from Eq. (21). The inset shows the dependence of β_E^{-1} on I_B obtained from the numerical simulation at $E_J = 10$ μeV ; the fitted line indicates $I_{B-H} = 0.16$ nA.

where the parameters inside the exponent are absorbed in κ . Thus, we arrive at an exponential dependence of I_{B-H} with E_J^2 :

$$\frac{I_{B-H}}{e} \propto \frac{\Gamma_{se\uparrow} + \exp(-\kappa E_J^2)}{\sqrt{1 + \Gamma_B^2/E_J^4}},$$

which is Eq. (21) in the main text. The effect of single-electron tunneling reflects on the bifurcation threshold curve through the saturation of $I_{B-H} (\neq 0)$ at higher- E_J values.

We have used Eq. (21) to fit the bifurcation threshold diagram. We find good agreement with both experimental and simulated data (cf. Figs. 7 and 9). Although our simulated threshold values deviate from our experimental E_J 's, we find similar functional tendency in the curves. Both in the simulation and experiment we observe that the bifurcation takes place earlier in the “inverted” regime than in the “normal” operation. In the inset of Fig. 9, we display a calculated β_E^{-1} versus I_B plot at $E_J = 10$ μeV . In the simulation, we also found a minimum E_J below which there is no bifurcation. Hence, we can conclude that our simulation quite well explains the experimental findings.

APPENDIX B: I_B VS β_E

According to Eq. (18),

$$\beta_E^{-1} = \frac{R_C}{V_C} \frac{e^2 \langle N_e' \rangle^2}{\tau_\uparrow (\tau_\uparrow + \tau_\downarrow)} \frac{1}{\langle I_B \rangle} (1 - \beta_H). \quad (\text{B1})$$

By inserting β_H from Eq. (A6), we reach the approximate form of β_E near the bifurcation threshold:

$$\beta_E^{-1} = \left[\frac{V_C \langle I_B \rangle \tau_\uparrow (\tau_\uparrow + \tau_\downarrow)}{R_C e^2 \langle N_e' \rangle^2} \frac{1}{1 - \frac{e}{\langle I_B \rangle} \left(\frac{e \langle N_e' \rangle}{\tau_\downarrow} + \epsilon \right)} \right]^{-1} \\ = \left[\frac{R_C \tau_\uparrow + \tau_\downarrow}{V_C \tau_\downarrow} (-\langle I_B \rangle + I_{B-H}) \right],$$

where I_{B-H} denotes the bifurcation threshold current. The above formulation is valid only in the vicinity of the divergence point, where the dominant change in β_E^{-1} can be viewed as linear in $\langle I_B \rangle$.

¹M. H. Devoret, J. M. Martinis, and J. Clarke, *Phys. Rev. Lett.* **55**, 1908 (1985).

²M. Tinkham, *Introduction to Superconductivity*, 2nd ed. (McGraw-Hill, New York, 1996).

³D. B. Haviland, L. S. Kuzmin, P. Delsing, K. K. Likharev, and T. Claeson, *Z. Phys. B* **85**, 339 (1991).

⁴L. S. Kuzmin and D. B. Haviland, *Phys. Rev. Lett.* **67**, 2890 (1991).

⁵D. V. Averin and K. K. Likharev, in *Mesoscopic Phenomena in Solids*, edited by B. L. Altshuler, P. A. Lee, and R. A. Webb (Elsevier, Amsterdam, 1991), p. 173.

⁶K. K. Likharev and A. B. Zorin, *J. Low Temp. Phys.* **59**, 347 (1985); D. V. Averin, A. B. Zorin, and K. K. Likharev, *Zh. Eksp. Teor. Fiz.* **88**, 692 (1985) [*Sov. Phys.-JETP* **61**, 407 (1985)].

⁷J. Delahaye, J. Hassel, R. Lindell, M. Sillanpää, M. Paalanen, H. Seppä, and P. Hakonen, *Science* **299**, 1045 (2003).

⁸J. Hassel and H. Seppä, *IEEE Trans. Appl. Supercond.* **11**, 260 (2001).

⁹J. Hassel, H. Seppä, J. Delahaye, and P. Hakonen, *J. Appl. Phys.* **95**, 8059 (2004).

¹⁰M. H. Devoret, D. Esteve, H. Grabert, G.-L. Ingold, H. Pothier, and C. Urbina, *Phys. Rev. Lett.* **64**, 1824 (1990).

¹¹T. Holst, D. Esteve, C. Urbina, and M. H. Devoret, *Phys. Rev. Lett.* **73**, 3455 (1994).

¹²J. Hassel and H. Seppä, *J. Appl. Phys.* **97**, 023904 (2005).

¹³G. Schön and A. D. Zaikin, *Phys. Rep.* **198**, 237 (1990).

¹⁴R. J. Prance, H. Prance, T. P. Spiller, and T. D. Clark, *Phys. Lett. A* **166**, 419 (1992).

¹⁵D. J. Flees, S. Han, and J. E. Lukens, *Phys. Rev. Lett.* **78**, 4817 (1997).

¹⁶R. Lindell, J. Penttilä, M. Sillanpää, and P. Hakonen, *Phys. Rev. B* **68**, 052506 (2003).

¹⁷C. Zener, *Proc. R. Soc. A* **137**, 696 (1932); **145**, 523 (1934).

¹⁸E. Ben-Jacob, Y. Gefen, K. Mullen, and Z. Schuss, *Phys. Rev. B* **37**, 7400 (1988).

¹⁹K. Mullen, Y. Gefen, and E. Ben-Jacob, *Physica B (Amsterdam)* **152**, 172 (1988).

²⁰K. Mullen, E. Ben-Jacob, and Z. Schuss, *Phys. Rev. Lett.* **60**, 1097 (1988).

²¹D. V. Averin, Yu. V. Nazarov, and A. A. Odintsov, *Physica B (Amsterdam)* **165&166**, 945 (1990).

²²S. M. Girvin, L. I. Glazman, M. Jonson, D. R. Penn, and M. D. Stiles, *Phys. Rev. Lett.* **64**, 3183 (1990).

²³G.-L. Ingold and Yu. V. Nazarov, in *Single Charge Tunneling*, edited by H. Grabert and M. H. Devoret (Plenum, New York, 1992), p. 21.

²⁴A. D. Zaikin and D. S. Golubev, *Phys. Lett. A* **164**, 337 (1992).

²⁵J. Delahaye, J. Hassel, R. Lindell, M. Sillanpää, M. Paalanen, H. Seppä, and P. Hakonen, *Physica E (Amsterdam)* **18**, 15 (2003).

- ²⁶Large line capacitance C_B leads to effective voltage bias at the base for small, high-frequency charge transfer relevant to the dynamics of the device, although current bias prevails at low frequencies.
- ²⁷R. Lindell, L. Korhonen, A. Puska, and P. Hakonen, *J. Low Temp. Phys.* **157**, 6 (2009).
- ²⁸J. S. Penttilä, Ü. Parts, P. J. Hakonen, M. A. Paalanen, and E. B. Sonin, *Phys. Rev. B* **61**, 10890 (2000).
- ²⁹M. A. Sillanpää, T. T. Heikkilä, R. K. Lindell, and P. J. Hakonen, *Europhys. Lett.* **56**, 590 (2001).
- ³⁰L. S. Kuzmin, Y. A. Pashkin, D. S. Golubev, and A. D. Zaikin, *Phys. Rev. B* **54**, 10074 (1996).
- ³¹R. K. Lindell and P. J. Hakonen, *Appl. Phys. Lett.* **86**, 173507 (2005).
- ³²J. Sarkar, A. Puska, J. Hassel, and P. J. Hakonen, *Supercond. Sci. Technol.* **26**, 065009 (2013).